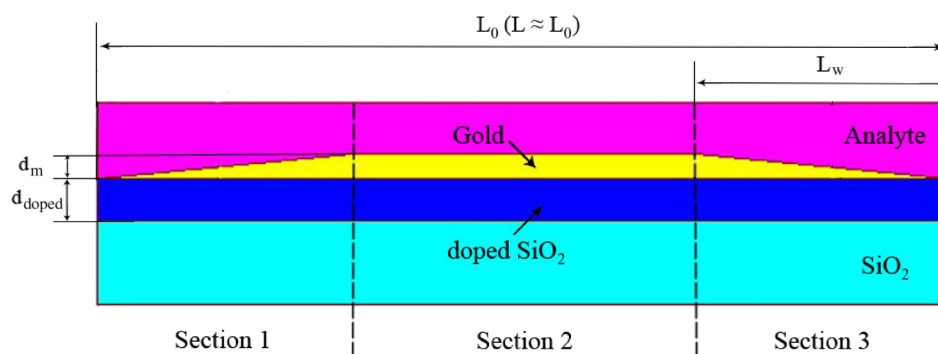


Surface Plasmon Interferometer Based on Wedge Metal Waveguide and Its Sensing Applications

Volume 4, Number 1, February 2012

Yang Ming
Zi-jian Wu
Hao Wu
Fei Xu
Yan-qing Lu, Senior Member, IEEE



DOI: 10.1109/JPHOT.2012.2186562
1943-0655/\$31.00 ©2012 IEEE

Surface Plasmon Interferometer Based on Wedge Metal Waveguide and Its Sensing Applications

Yang Ming, Zi-jian Wu, Hao Wu, Fei Xu, and Yan-qing Lu, *Senior Member, IEEE*

College of Engineering and Applied Sciences and National Laboratory of Solid State Microstructures, Nanjing University, Nanjing 210093, China

DOI: 10.1109/JPHOT.2012.2186562
1943-0655/\$31.00 ©2012 IEEE

Manuscript received December 28, 2011; revised January 23, 2012; accepted January 25, 2012. Date of current version February 17, 2012. This work was supported by 973 programs under Contract 2010CB327803, Contract 2011CBA00200, and Contract 2012CB921803, the National Science Foundation of China under Programs 11074117 and 60977039, the Priority Academic Program Development of Jiangsu Higher Education Institutions, and Fundamental Research Funds for the Central Universities. Corresponding author: Y. Lu (e-mail: yqlu@nju.edu.cn).

Abstract: We propose a surface plasmon interferometer based on a wedge metal waveguide. Working principles of the device are introduced through theoretical analyses. The interference performances are investigated by finite-difference time-domain (FDTD) method. Because of the special wedge geometry, the interferometer shows an extremely low coupling loss in comparison with the previous reports. An interesting surface plasmon polariton (SPP) coupling and splitting phenomenon is found at the wedge section. It is then split into two surface plasmon modes in two interference arms. Refractive index sensing applications of this interferometer are also discussed, which shows sensitivity as high as 6×10^3 nm/RIU.

Index Terms: Sensors, plasmonics.

1. Introduction

Surface plasmon polariton (SPP) is a transverse-magnetic surface electromagnetic excitation propagating at the interface of a metal and a dielectric [1]. To date, various SPP excitation schemes have been demonstrated, including prism coupling [2], grating coupling [3], optical waveguide based [4], enhanced transmission through nanohole arrays [5], and resonance of nanoparticles [6]. Utilizing the unique characteristics of SPP, people have proposed and demonstrated many applications in sensing [2]–[6], spectroscopy [7], and nonlinear optics [8], [9]. Up to date, different kinds of surface plasmon resonance (SPR) sensors have been successfully commercialized. Owing to the unique capability of SPP to confine the electromagnetic field in the perpendicular direction, SPR sensors could principally be fabricated in an extremely small size and with high sensitivity. Recently, a new type of SPP interference sensor was proposed and has attracted plenty of attention [10]–[15]. A metal film section is deposited on or partly buried in a dielectric waveguide; therefore, the excited SPP modes at the top and bottom of the metal film thus may interfere with each other for sensing or modulation applications [10]. However, because of the impedance mismatch, the waveguide mode to SPP coupling normally suffers a high loss, at least for one of the SPP modes.

In this paper, we proposed a plasmonic Mach–Zehnder interferometer that consists of a wedge metal waveguide on a silica substrate. Because of the gradient transition from the waveguide mode to the “coupled SPP” mode, the light to SPP coupling thus exhibits a very low loss. The mode

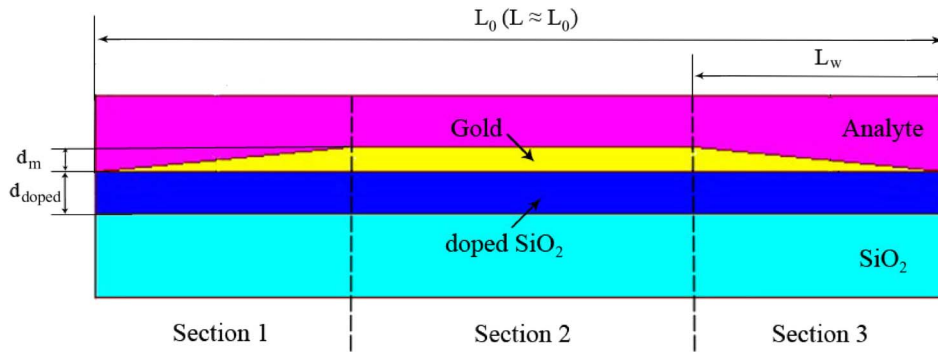


Fig. 1. Structure of the proposed surface plasmon interferometer.

coupling, splitting, and interference characteristics are investigated theoretically by using FDTD analysis. Applications of our SPP interferometer for refractive index sensing are also studied showing a sensitivity of 6×10^3 nm/RIU. Our whole paper contains four parts. The basic theory part is introduced in Section 2, including the working principle, the characterizations, and advantages of our proposal. In Section 3, the sensing application of the SPP interferometer is discussed based on numerical simulations. Structural parameters are optimized to improve the sensitivity of our sensor. Finally, conclusions are given in Section 4.

2. Theory of the Interferometer

The basic structure of our SPP interferometer is shown in Fig. 1. It consists of a silica substrate with a doped high index top layer. A section of wedgy gold film is further deposited on it whose thickness is gradually varied on both side slopes. The silica-on-silicon substrate could be prepared by plasma-enhanced chemical vapor deposition (PECVD) technology [16] or flame hydrolysis deposition (FHD) technology [17]. To make the wedge film, a simple mechanical setup could be used to control the gold deposition region [18]. The detailed scheme could be as follows: Put a cover with a rectangle slot over the substrate. Move the cover left and right periodically during film deposition. Therefore, the center area of the slot has a uniform and thicker gold layer, while the two side slopes have gradually varied thickness. It is not difficult to obtain such a wedgy gold film with different length, slope, and thickness.

In our simulation, the dielectric constant of gold is determined from the Drude model with the plasma frequency $\omega_p = 2\pi \times 2.175 \times 10^{15} \text{ s}^{-1}$ and the collision frequency $\omega_c = 2\pi \times 6.5 \times 10^{12} \text{ s}^{-1}$ [19]. To simplify the calculations, the dispersion of the silica substrate is neglected. We set the refractive index of the doped silica core and the pure silica buffer to be 1.53 and 1.50, respectively. We divide the device into three sections: The left wedge area acts as an input waveguide, the flat area is mainly for Mach–Zehnder interference, and the right wedge area is the output waveguide. When a guiding mode supported by the silica-on-silicon waveguide was launched into the first wedge section, it could be split into two SPP modes: the top SPP mode and the bottom SPP mode. Obviously, the wedge thickness should be large enough to separate two SPP modes before they enter the two interferometer arms in Section 2. In addition, the thickness of the bottom doped silica layer should be chosen properly to ensure that the lower arm only supports one mode, i.e., the bottom SPP mode.

The basic working principle of the surface plasmon interferometer is not hard to understand. It just looks like the traditional ones. The interference is provided by the phase difference between the two arms. In addition, the wedge section also contributes a tiny beam path difference, but of course, it is not the main part. The dominating part should still be the difference of the phase velocity in different arms, which is determined by the propagation constant ($\beta = 2\pi/\lambda \sqrt{\epsilon'_{\text{gold}} n^2 / (\epsilon'_{\text{gold}} + n^2)}$) and the frequency of the SP wave. In our theoretical study, the propagation constant of the top and bottom SPP modes are both deduced from the equation above for simplicity. This is only valid when the

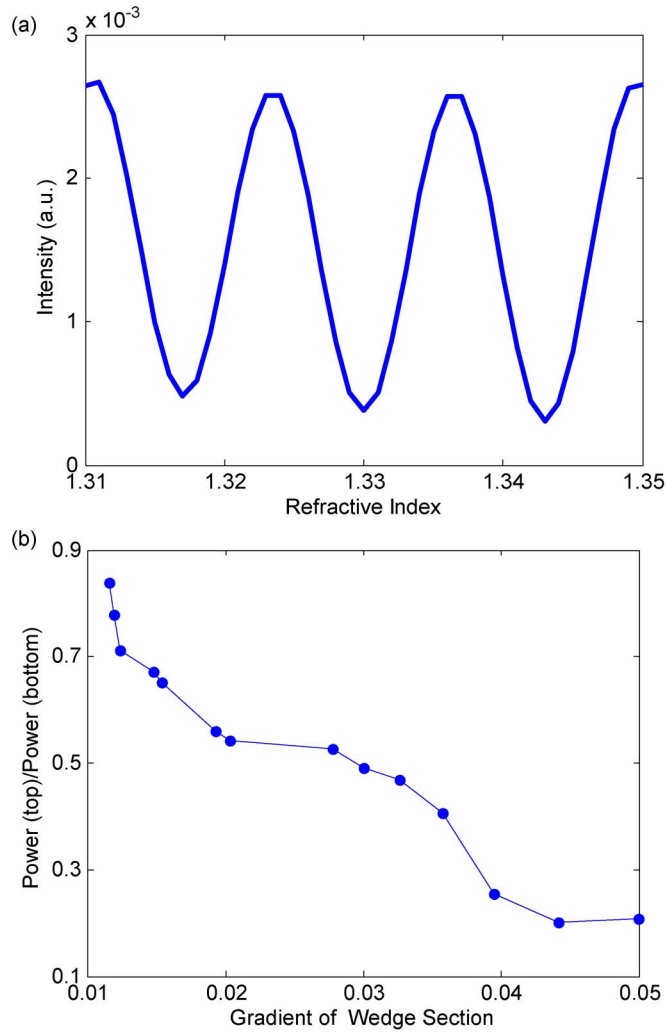


Fig. 2. (a) Simulated spectrum of an SPP interferometer. (b) Power ratio of top SP mode and bottom SP launched into Section 2.

thickness of the doped silica layer is large enough. Otherwise, the bottom SPP mode may give an inaccurate result. A more general three layer waveguide model should be used instead [20]. For a fixed wavelength, the refractive index difference of the substrate and the environment dominates the propagation constants of the top mode and the bottom mode. When they couple back into the output waveguide, relative phase difference of the two modes results in interference and a sinusoidal spectrum [11]

$$I = |E|^2 = I_1 + I_2 + 2\sqrt{I_1 I_2} \cos \left[\frac{2\pi L}{\lambda} \left(\sqrt{\frac{\epsilon'_{\text{gold}} n_{\text{env}}^2}{\epsilon'_{\text{gold}} + n_{\text{env}}^2}} - \sqrt{\frac{\epsilon'_{\text{gold}} n_{\text{bas}}^2}{\epsilon'_{\text{gold}} + n_{\text{bas}}^2}} \right) \right] \quad (1)$$

where ϵ'_{gold} stands for the real part of dielectric constant of gold, and n_{env} and n_{bas} are the environmental index and the refractive index of bottom doped silica layer, respectively. L is the total interference length. When phase difference of the top mode and the bottom mode is 0 or π , they will interfere constructively or destructively to provide the maximum or minimum of the intensity, respectively. To improve the visibility of the interferometer, we should regulate the structural

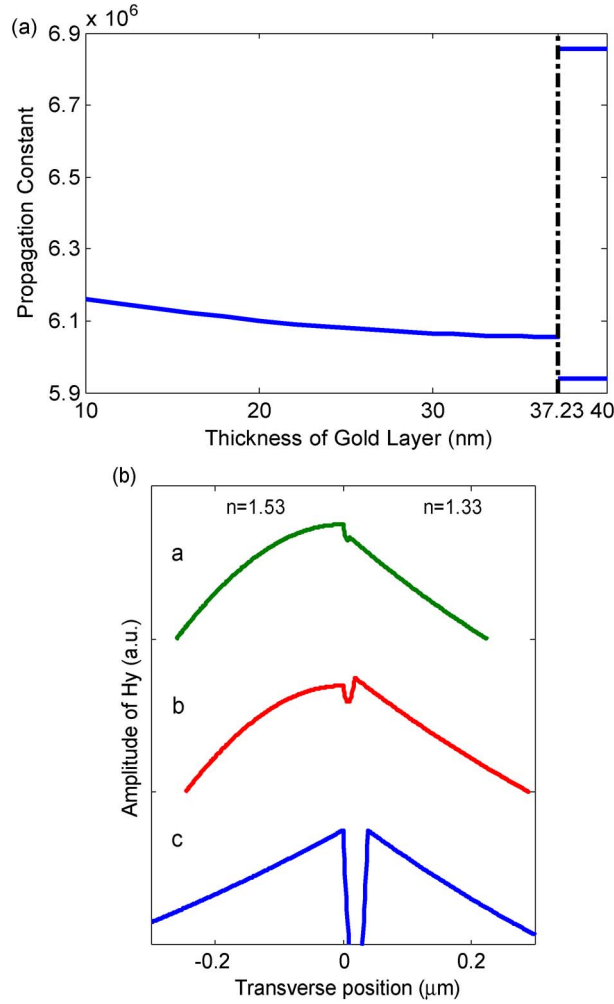


Fig. 3. (a) Propagation constant varies with the thickness of gold layer. When the thickness increases to 37.23 nm, the “coupled-SPP” mode splits into two modes. (b) Splitting process of the mode, the Au layer thickness of a, b, and c positions are 11 nm, 18 nm, and 39 nm, respectively.

parameters of the device to make the minimum be as close to zero as possible. The governing functions are as follows [14], [15]:

$$2(\phi_{b0} - \phi_{t0}) - \text{Re}(\beta_b - \beta_t)L = (2m + 1)\pi \quad (2)$$

$$\left| \frac{T_b}{T_t} \right|^2 = \left| \frac{A_b}{A_t} \right|^2 \exp[-\text{Im}(\beta_b - \beta_t)L] \quad (3)$$

where ϕ_{b0} and ϕ_{t0} are the phase differences introduced by the coupling processes. T_b and T_t stand for transmission amplitude of the top SPP mode and the bottom SPP mode coupled into the output silica-on-silicon waveguide, while A_b and A_t represent the initial field amplitudes of the top and bottom SPP modes, respectively. β_b and β_t are the respective propagation constants of the two SPP modes and they have negative imaginary parts related to their large propagation loss.

In practice, there are three structural parameters that we need to take into account: the total length of three sections (L_0), the thickness of the doped silica layer (d_{doped}), and the gradient of the wedge section ($g_m(d_m, L_w)$), which is defined as the ratio of the gold film thickness in Section 2 (d_m) and the length of Section 1 (L_w). In our simulation, we assume $L_0 = 100 \mu\text{m}$, $d_{\text{doped}} = 1 \mu\text{m}$, and

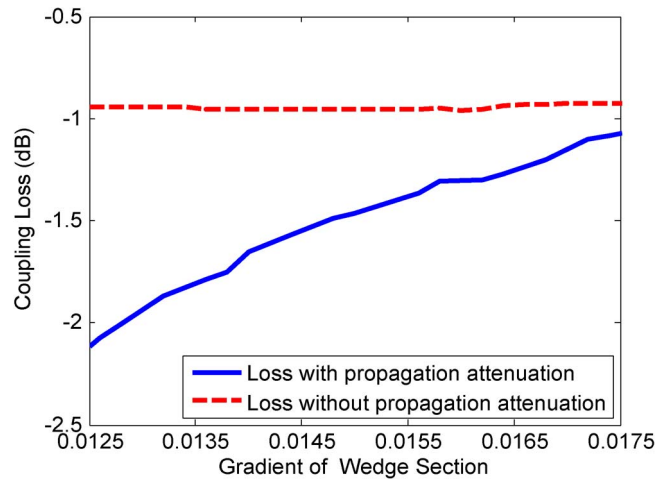


Fig. 4. Total coupling loss of the interferometer to the top and bottom SPP mode as a function of the gradient of wedge section.

$g_m = 0.015$ ($d_m = 150$ nm, $L_w = 10$ μ m). The interference is shown in Fig. 2(a), while Fig. 2(b) reflects the power ratio between the top and bottom SPP modes. The input TM mode light power is redistributed into two SPP modes, exhibiting a clear mode splitting effect. As is shown in the picture, the proportion of the power launched into top SPP mode decreases with g_m . Owing to this effect, a proper splitting ratio could be obtained easily by tuning the structural parameters.

In the interference process, when the input guiding mode is launched into the wedge metal waveguide, it could excite a metastable “coupled SPP” mode. This mode behaves like a long-range surface plasmon mode. However, because of the large mismatch of two sides’ refractive index, it could not propagate stably and is split into two independent SPP modes quickly, i.e., the top and the bottom SPP modes. An analytic three layer waveguide model [20] is used to study the generation and splitting of this coupled mode as shown in Fig. 3. When the gold layer is thinner than 37.23 nm, there is only one mode with light field on both sides of the film. Fig. 3(b) shows the splitting process of the mode, position “a” corresponds to the position where the thickness of Au layer is 11 nm, and the field has hardly split. The thickness of Au layer of position “b” is 18 nm, and the splitting has happened. Position “c” corresponds to a total splitting of the mode with a thickness of 39 nm. If the gold film thickness is larger than 39 nm, the top and bottom SPP modes are more separated with different propagation constants. As a consequence, the interference length L does not just mean the total length of three sections. It is the length of the total effective interference path after the “coupled SPP” mode is split and before the split top and bottom modes are recombined in Section 3. However, because the “coupled SPP” mode is just a transition state with only nanometer scale propagation length, L is almost equal to the total length of three sections (L_0), as shown in Fig. 1.

Owing to the “coupled SPP” mode, the total interference process is a continuously varying process, and therefore, losses arisen from uncontinuity of the structure could be avoided. Coupling loss of the interferometer which is defined by the ratio of total power of two SPP modes, and the input power is shown in Fig. 4. Corresponding to $g_m = 0.0125$, the coupling loss is about 2 dB. As g_m gets larger, the loss becomes lower. It even reduces to below 1 dB when g_m increases to 0.0175. It is worth noticing that the propagation attenuation caused by the imagined part of the propagation constant is included, and therefore, the coupling loss of smaller g_m which has a longer coupling section is larger. To have a clearer physical image, we remove this portion by follow-up theoretical treatment. It could be seen that the loss is even smaller. Overall, the total coupling loss is much lower compared with previous reports [10].

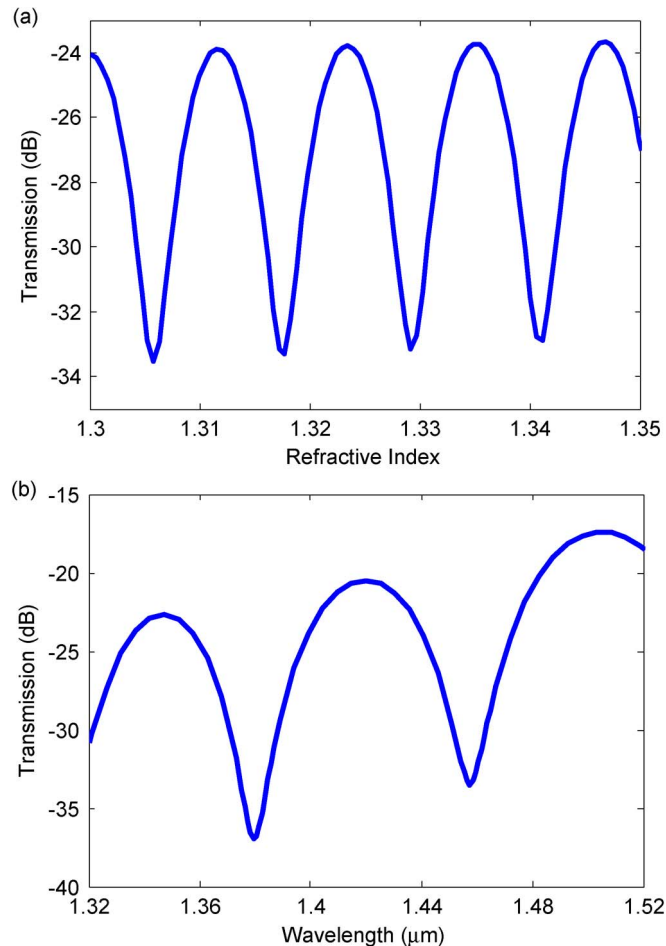


Fig. 5. (a) Transmission of the surface plasmon interferometer sensor as a function of refractive index. The working wavelength is fixed at $1.4 \mu\text{m}$. (b) Transmission of the surface plasmon interferometer sensor as a function of wavelength. The refractive index of the water sample is set to be 1.33.

3. Sensing Applications

The surface plasmon interferometer proposed above has many applications. As an example, we would study its refractive index sensing properties. The top interference path and the bottom interference path are treated as the sensing arm and the reference arm, respectively. When the environmental refractive index changes, the propagation constant of the top SPP mode varies accordingly. However, the propagation constant of the bottom SPP mode is insensitive, and therefore, the relative phase difference of the two modes is the function of environment refractive index. This effect drives the device to be sensitive to variation of environment index, and correspondingly, the transmission spectrum of the device will present a shift. The shift of valleys in the spectrum is usually used for sensing. Furthermore, in a practical device, the analyte should cover at least the total interference length L , and because of the field penetration outside the gold film, the analyte's thickness should be large enough to take all top SPP field. From our simulation, a $> 2 \mu\text{m}$ -thick analyte is suitable with almost all fields included. Otherwise, an analyte that is too thin may result in a lower sensitivity.

Simulations of our device are carried out by the commercial software Rsoft CAD-Layout through the finite-difference time-domain (FDTD) method. We use the 2-D model in our simulations, and the numerical parameters of spatial meshes are $0.03 \mu\text{m}$ in the transverse direction and $0.1 \mu\text{m}$ in the propagation direction, respectively. In our calculations, the three structural parameters of the

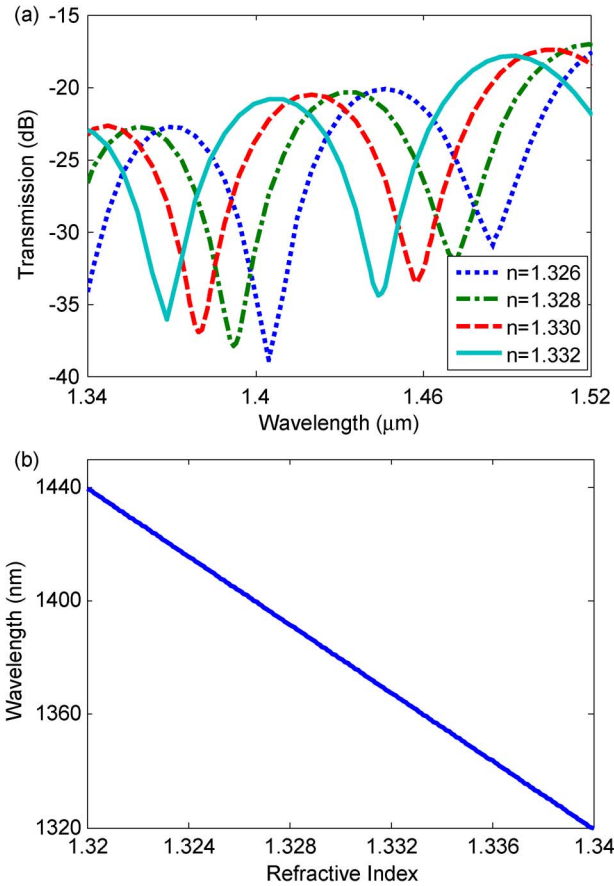


Fig. 6. (a) Transmission spectra for refractive index 1.326, 1.328, 1.330, and 1.332 of the sample. (b) Transmission minimum as a function of environmental refractive index.

interferometer sensor mentioned above should be optimized to for better sensing performances. Among these parameters, influence of the total length L is expressed directly in (2) and (3). It plays a more important role because the peak positions of the transmission spectrum of the device are determined mainly by it. Besides, another parameter of the sensor, i.e., the FSR is the function of L ($\text{FSR} \approx \lambda^2 / \Delta n_{\text{eff}} L$). As L becomes larger, the FSR will be shorter with a sharper transmission valley. The full-width at half-maximum (FWHM) power thus will be reduced, and the Q-factor ($Q = \lambda / \text{FWHM}$) of the sensor will be improved. In addition, d_{doped} affects T_b and T_t at the same time, while smaller g_m results in a larger T_t . The ratio $|T_b / T_t|^2$ thus could be tuned accurately by adjusting these two parameters, together with the total length L . An index sensor with optimized performances thus could be obtained according to different application requirements.

Fig. 5 shows the performance of an SPP interferometer with $L_0 = 114.6 \mu\text{m}$ for the total length, $d_{\text{doped}} = 1.15 \mu\text{m}$ for the waveguide layer thickness, and $g_m = 0.012$ ($d_m = 150 \text{ nm}$, $L_w = 12.15 \mu\text{m}$) for the wedge gradient, respectively. The transmission which is defined by (1) is plotted as a function of refractive index and wavelength in Fig. 5(a) and (b), respectively. In Fig. 5(a), the wavelength is fixed at $1.4 \mu\text{m}$; and in Fig. 5(b), the environmental refractive index of the sample is set at 1.33, i.e., the index of water.

Fig. 5(a) displays the interference characteristics of the sensor. Relative phase of the top and bottom modes varies rapidly with the refractive index. According to Fig. 5(a), the resonance period is ~ 0.012 , i.e., a 2π phase difference can be brought by a tiny variation of refractive index. Fig. 5(b) shows the wavelength response of the sensor. We can see that for our device, FSR is $\sim 78 \text{ nm}$, and FWHM is $\sim 21 \text{ nm}$. Combining two types of properties to estimate, the high sensitivity of our device could be predicted.

For sensing applications, the regime which is called “wavelength interrogation mode” [10] is usually more useful. We calculate the transmission spectrums for refractive index of 1.326, 1.328, 1.330, and 1.332, and the data are collected together and shown in Fig. 6(a). Further calculations are also made to obtain sensitivity of our device. Fig. 6(b) shows the position of the resonance wavelength which corresponds to transmission minimum as a function of sample refractive index.

From Fig. 6(b), we could see that wavelength at transmission minimum reduces linearly against sample refractive index improving. The sensitivity of the device is around 6.0×10^3 nm/RIU. This sensitivity could also be estimated by theoretical analyses. As mentioned above, the analytic expression of the bottom SPP mode is also used in the derivation here. Controlling equations are given as follows [11], [13]:

$$S = \frac{\Delta\lambda}{\Delta n} = \frac{\lambda}{n_{\text{top}}^3} \left(\sqrt{\frac{\epsilon'_{\text{gold}} n_{\text{top}}^2}{\epsilon'_{\text{gold}} + n_{\text{top}}^2}} \right)^{3/2} / \left[\sqrt{\frac{\epsilon'_{\text{gold}} n_{\text{top}}^2}{\epsilon'_{\text{gold}} + n_{\text{top}}^2}} - \sqrt{\frac{\epsilon'_{\text{gold}} n_{\text{bot}}^2}{\epsilon'_{\text{gold}} + n_{\text{bot}}^2}} \right]. \quad (4)$$

Assuming $\lambda = 1.40 \mu\text{m}$, the sensitivity is calculated to be 6.9×10^3 nm/RIU, and the difference is introduced in by the approximations used to derivate the expression of sensitivity and the error brought by the numerical method itself.

In both direct data fitting or theoretical analysis, our sensor show a much higher sensitivity than some previous reported results. However, this is mainly because of the different material system, and therefore, the direct comparison is difficult. We use a doped Silica waveguide while a Silicon-on-insulator substrate was normally employed before [10]. Both of these two approaches have advantages and disadvantages. For example, our sensor shows a long device length (over $100 \mu\text{m}$), but a more compact $\sim 10 \mu\text{m}$ SPP sensor was reported in [10]. Therefore, our sensor requires a larger amount of analyte. This is one drawback of the present sensor. However, the longer device results in finer spectrum with shorter FSR/FWHM. So, the L value should be well selected according to different applications. Although we set a long L , it also could be smaller if a sensor with lower loss and larger sensing range is desired [21]. In addition, because L affects both the top and bottom SPP's attenuation while they are not identical, L is also a tuning factor to adjust the contrast of spectrum peaks and valleys according to (2) and (3). For our sensor, the spectrum contrast reaches around 20 dB, which is quite good.

4. Conclusion

We have presented in this paper a surface plasmon interferometer based on wedge metal waveguide. Working principles of this device are discussed through theoretical analyses. This is attributed to the special mode supported by the wedge metal waveguide, i.e., the “coupled SPP” mode. The total coupling loss of the interferometer is very low. Its applications for refractive index sensing are also investigated. Owing to characteristics of surface plasmon, the sensor has a really high sensitivity. The size of the device could be controlled as small as a micrometer order of magnitude, which makes it a promising candidate for nanophotonic integration.

References

- [1] H. Raether, *Surface Plasmons on Smooth and Rough Surfaces and on Gratings*. Berlin, Germany: Springer-Verlag, 1988.
- [2] G. G. Nenninger, P. Tobiska, J. Homola, and S. S. Yee, “Long-range surface plasmons for high-resolution surface plasmon resonance sensors,” *Sens. Actuators B, Chem.*, vol. 74, no. 1, pp. 145–151, Apr. 2001.
- [3] S. Y. Wu, H. P. Ho, W. C. Law, C. Lin, and S. K. Kong, “Highly sensitive differential phase-sensitive surface plasmon resonance biosensor based on the Mach–Zehnder configuration,” *Opt. Lett.*, vol. 29, no. 20, pp. 2378–2380, Oct. 2004.
- [4] J. Shibayama, “Three-dimensional numerical investigation of an improved surface plasmon resonance waveguide sensor,” *IEEE Photon. Technol. Lett.*, vol. 22, no. 9, pp. 643–645, May 2010.
- [5] A. G. Brolo, R. Gordon, B. Leathem, and K. L. Kavanagh, “Surface plasmon sensor based on the enhanced light transmission through arrays of nanoholes in gold films,” *Langmuir*, vol. 20, no. 12, pp. 4813–4815, May 2004.
- [6] J. J. Mock, D. R. Smith, and S. Schultz, “Local refractive index dependence of plasmon resonance spectra from individual nanoparticles,” *Nano Lett.*, vol. 3, no. 4, pp. 485–491, Mar. 2003.

- [7] C. Sönnichsen, S. Geier, N. Hecker, G. von Plessen, J. Feldmann, H. Ditlbacher, B. Lamprecht, J. Krenn, F. Ausseinnegg, V. Chan, J. Spatz, and M. Möller, "Spectroscopy of single metallic nanoparticles using total internal reflection microscopy," *Appl. Phys. Lett.*, vol. 77, no. 19, pp. 2949–2951, Nov. 2000.
- [8] Z. J. Wu, X. K. Hu, Z. Y. Yu, W. Hu, F. Xu, and Y. Q. Lu, "Nonlinear plasmonic frequency conversion through quasiphase matching," *Phys. Rev. B, Condens. Matter*, vol. 82, no. 15, p. 155 107, Oct. 2010.
- [9] F. F. Lu, T. Li, X. P. Hu, Q. Q. Cheng, S. N. Zhu, and Y. Y. Zhu, "Efficient second-harmonic generation in nonlinear plasmonic waveguide," *Opt. Lett.*, vol. 36, no. 17, pp. 3371–3373, Sep. 2011.
- [10] P. Debackere, S. Scheerlinck, P. Bienstman, and R. Baets, "Surface plasmon interferometer in silicon-on-insulator: Novel concept for an integrated biosensor," *Opt. Exp.*, vol. 14, no. 16, pp. 7063–7072, Aug. 2006.
- [11] X. Wu, J. Zhang, J. Chen, C. Zhao, and Q. Gong, "Refractive index sensor based on surface-plasmon interference," *Opt. Lett.*, vol. 34, no. 3, pp. 392–394, Feb. 2009.
- [12] P. Debackere, R. Baets, and P. Bienstman, "Bulk sensing experiments using a surface-plasmon interferometer," *Opt. Lett.*, vol. 34, no. 18, pp. 2858–2860, Sep. 2009.
- [13] Q. Q. Gan, Y. K. Gao, and F. J. Bartoli, "Vertical plasmonic Mach–Zehnder interferometer for sensitive optical sensing," *Opt. Exp.*, vol. 17, no. 23, pp. 20 749–20 755, Nov. 2009.
- [14] K. Q. Le and P. Bienstman, "Enhanced sensitivity of silicon-on-insulator surface plasmon interferometer with additional silicon layer," *IEEE Photon. J.*, vol. 3, no. 3, pp. 538–545, Jun. 2011.
- [15] M. S. Kwon, "Theoretical investigation of an interferometer-type plasmonic biosensor using a metal-insulator-silicon waveguide," *Plasmonics*, vol. 5, no. 4, pp. 347–354, Dec. 2010.
- [16] H. Ou, "Different index contrast silica-on-silicon waveguides by PECVD," *Electron. Lett.*, vol. 39, no. 2, pp. 212–213, Jan. 2003.
- [17] A. Kilian, J. Kirchhof, B. Kuhlow, G. Przyrembel, and W. Wischmann, "Birefringence free planar optical waveguide made by flame hydrolysis deposition (FHD) through tailoring of the overcladding," *J. Lightw. Technol.*, vol. 18, no. 2, pp. 193–198, Feb. 2000.
- [18] M. R. Witzman, R. A. Bradley, C. W. Lantman, and E. R. Cow, "Linear aperture deposition apparatus and coating process," U.S. Patent 6 202 591 B1, Mar. 20, 2001.
- [19] S. Linden, C. Enkrich, M. Wegener, J. Zhou, T. Koschny, and C. M. Soukoulis, "Magnetic response of metamaterials at 100 Terahertz," *Science*, vol. 306, no. 5700, pp. 1351–1353, Nov. 2004.
- [20] G. Lifante, *Integrated Photonics: Fundamentals*. Chichester, U.K.: Wiley, 2003.
- [21] S. Y. Zhang, Q. Zhong, X. S. Qian, X. W. Lin, F. Xu, W. Hu, and Y. Q. Lu, "A three-beam path photonic crystal fiber modal interferometer and its sensing applications," *J. Appl. Phys.*, vol. 108, no. 2, p. 023107, Jul. 2010.